

Model System Supported Impedance Simulation of Composite Electrodes

A. K. Opitz^{1,2}*, M. Gerstl^{1,2}, M. Bram²

- ¹ TU Wien, Institute of Chemical Technologies and Analytics, Getreidemarkt 9/164-EC, 1060 Wien, Austria
- ² Christian Doppler Laboratory for Metal-Supported Electrochemical Energy Converters, Forschungszentrum Jülich GmbH, Institute of Energy and Climate Research, Materials Synthesis and Processing (IEK-1), Wilhelm-Johnen-Strasse, 52425 Jülich, Germany

Received December 06, 2018; accepted July 02, 2019; published online July 17, 2019

Abstract

Current research on fuel electrodes of solid oxide cells (SOCs) is done either on model-type pattern electrodes or by interpretation of impedance spectra measured on "real" porous paste electrodes. However, results obtained by both methods are not always straightforward to compare. To bridge this gap, in this study impedance spectra of 3D porous composite electrodes with a well-defined geometry are simulated using elementary parameters from model-type experiments. By independent variation of these elementary parameters, it is possible to analyze the influence of the individual elementary processes on the overall electrode performance without the issue of changing its microstructure, which usually occurs when changing materials in case of real porous electrodes.

The obtained results identify the electrochemical reaction resistance as the parameter with the highest impact on the polarization resistance of porous electrodes. This study thus provides a basis for a knowledge-based improvement of existing and novel composite fuel electrodes.

In addition, the developed transmission line model is used for critically examining the common method of deconvolution of impedance data measured on real porous composite electrodes, which often relies on the assumption of elementary processes being represented by a serial connection of simple $R \mid C$ elements.

Keywords: Cermet Anode, Deconvolution of Impedance Spectra, Microstructure, Ni/GDC, Ni/YSZ, Polarization Resistance, SOFC

1 Introduction

Solid oxide cells (SOCs) provide a very efficient way of directly converting chemically bound energy to electricity (solid oxide fuel cells, SOFCs) and *vice versa* (solid oxide electrolysis cells, SOECs). Due to their elevated operating temperature, this type of cells offers rather wide fuel flexibility from hydrogen to hydrocarbon-based fuels or alcohols, thus making them compatible to the existing fuel infrastructure [1–7]. Owing to this fuel flexibility, SOCs can play important roles in future energy supply scenarios: (i) SOFCs for stationary electricity generation [4,8], (ii) metal-supported SOFCs for mobile applications [9–13], and (iii) SOECs for storage of excess electricity in the form of chemical bonds [2, 14–16].

For all three cases, a deeper fundamental understanding of the electrochemical processes and the reaction kinetics of the fuel electrodes is needed to increase the power density and long term stability of SOCs thus enabling them to commercially compete with existing systems such as combustion engines. In this context, the following issues have to be addressed: (i) for stationary SOFC applications, H2S induced performance losses of the fuel electrode need to be minimized to reach cell lifetimes above 40,000 h [1, 4, 17-19], (ii) in case of metal-supported SOFCs - due to the sintering process in reducing environment – the anode suffers from a suboptimal microstructure, which constitutes an obstacle on the way to higher power densities [4,9,12,20], (iii) running Ni/YSZ fuel electrodes in electrolysis mode makes them prone to microstructural changes, which leads to an electrochemical performance loss of SOECs [3,14]. To develop efficient counter strategies for the electrode-related performance issues the complex interplay of electrochemical elementary processes

[►] Paper presented at the 13th EUROPEAN SOFC & SOE Forum (EFCF2018), July 3–6, 2018 held in Lucerne, Switzerland. Organized by the European Fuel Cells Forum www.efcf.com

^[*] Corresponding author, alexander.opitz@tuwien.ac.at

This is an open access article under the terms of the Creative Commons Attribution License, which permits use, distribution and reproduction in any medium, provided the original work is properly cited.

and the microstructure of the fuel electrode needs to be well-understood.

Characterization of relevant electrochemical processes on Ni-based fuel electrodes is mainly done by two different approaches. One approach employs micro-patterned model electrodes for fundamental investigations of elementary processes [21-26]. Since geometrical properties of these electrodes can be tailored rather easily, microelectrodes are also a very powerful tool for investigating different electrochemical reaction pathways [27,28]. The second approach relies on deconvolution of impedance spectra obtained on "real" porous cermet electrodes with the aim of separating individual processes [3, 17, 29-37]. Unfortunately, due to the completely different geometry of model-type pattern electrodes and porous cermets the results on both systems can often be only compared with difficulties. Therefore, the knowledge gained on modelelectrodes has so far only slowly appeared in the interpretation of impedance results of cermet electrodes and only very few studies strive for a physically all-embracing interpretation of impedance data obtained on "real" porous electrodes [24, 38, 39].

As an illustration for the fundamental problem of comparability between strongly simplified model electrodes and "real" porous cermets the question of predicting the electrochemical performance change for the case of changing the ion conducting phase in a cermet should be briefly discussed. This question is particularly interesting since Ni/ceria based cermets have been shown to be a promising alternative to Ni/yttria-stabilized zirconia (YSZ) fuel electrodes, especially for intermediate temperature cells [7, 40–42]. However, the reasons for the superior electrochemical performance of Ni/ceria cermets are mechanistically not completely understood, since definitely more than one property is changed when using Gd or Sm doped ceria (GDC or SDC) instead of YSZ:

- (i) The ionic conductivity in the cermet is increased [43, 44].
- (ii) Ceria, in contrast to YSZ, exhibits additional electronic conductivity under H₂/H₂O atmospheres, which leads to a completely different electrochemical reaction mechanism [45, 46]. While the reaction on Ni/YSZ predominantly occurs close to the triple phase boundary (TPB) [22, 23], the electrochemically active region is largely extended along the free GDC/SDC surface [47-49]. Both situations are sketched for model-type thin film electrodes in Figure 1; the red highlighted parts indicate the regions of electrochemical activity. For obtaining geometry normalized elementary parameters, these different reaction sites lead to length-related resistances in case of Ni/YSZ and to area-related resistances in case of Ni/GDC or Ni/SDC. Therefore, the question which cermet will be electrochemically more active cannot be straightforwardly answered from these model experiments.
- (iii) In addition, also the microstructure of the respective cermets plays an important role. Owing to different sintering behavior of YSZ and GDC/SDC as well as to different wetting behavior of Ni on these oxides, the microstructure

of the Ni/YSZ and Ni/ceria cermets can be expected to be also significantly different [12,50]. This additional difference makes prediction of electrochemical performance even more challenging.

To bridge this gap between results from model and "real" porous electrodes the introduction of an intermediate level of abstraction is suggested in this contribution. This is done by simulation of impedance data for 3D porous composite electrodes with a geometrically well-defined microstructure. For this artificial porous electrode, a transmission line type equivalent circuit is employed considering the physical relationships of the contributing elementary processes on composite electrodes. With this transmission line model, the influence of the different elementary parameters such as ionic and electronic conductivity as well as electrochemical reactivity on the total polarization resistance of a porous composite electrode is studied without the issue of changing the microstructure of the electrode. This analysis reveals the electrochemical reactivity as the most impactful parameter for a performance increase of porous electrodes and thus yields valuable knowledge for developing improvement strategies for composite fuel electrodes.

2 Modeling Approach

The impedance model presented here is derived with the aim of representing the physically relevant elementary processes as well as their electrochemically correct connection for the case of a composite fuel electrode. On such a dual-phase electrode, two electrical pathways for ions and electrons are active, which are connected *via* the electrochemical reaction. Both phases can principally also show dielectric behavior, modeled by capacitors in both rails. Moreover, the electrode capacitance needs to be considered, which originates either from the electrochemical equilibrium at the phase boundary of

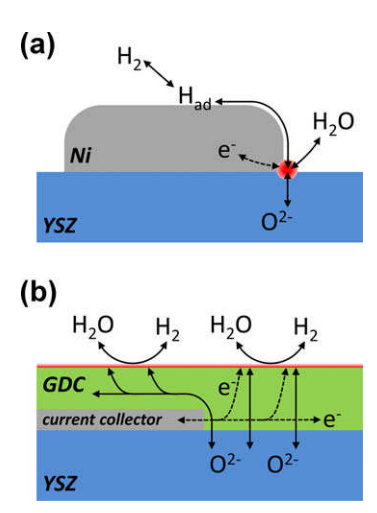


Fig. 1 Sketch of electrochemical reaction pathways on (a) micro-patterned Ni/YSZ model electrodes and (b) GDC model composite electrodes with embedded metallic current collectors. The red highlighted zones indicate the region where the electrochemical reaction takes place.

the two respective materials or from a chemical capacitance. (It should be noted that the dielectric capacitances in both rails are usually much smaller than the electrode capacitance and thus effects from these capacitors can only be observed at very high frequencies. Here, the dielectric capacitances are considered for the sake of completeness, but the capacitive behavior of the investigated cermets is almost exclusively governed by the electrode capacitance - see results.)

This situation is sketched for the example of a Ni/YSZ cermet electrode in H₂/H₂O atmosphere in Figure 2a: The percolating YSZ network serves as the ion conducting rail with the electrolyte as the ionic current collector. The percolating Ni phase is the electron conducting rail and the electronic current collector in case of a real SOC is either the substrate or the metallic interconnector. The electrochemical reaction couples the ionic to the electronic current and for Ni/YSZ this reaction is assumed to be restricted to the triple phase boundary (TPB). The same situation is sketched in a geometrically simplified version in Figure 2b. Here, the two pathways are established by two straight and geometrically well-defined columns of octagonal cross section contacting each other. The electrochemically active TPB in this case is indicated by the red line. A three dimensional visualization of the simplified cermet structure is depicted in Figure 2d.

From the available current pathways in the cermet electrode the equivalent circuit in Figure 2c is derived as follows: Along both ionic and electronic rail charge transport occurs either via a short range displacement polarization or via a long range current. The first process can be characterized by the

dielectric behavior of the materials and is represented by differential capacitors cx in the rails of the equivalent circuit in Figure 2c (x denotes the index "ion" or "eon"). The second process is characterized by the conductivity of the materials and is represented in the circuit by differential resistors r_x. These differential capacitors and differential resistors are connected to the absolute capacitances C_x and absolute resistances R_x as well as to the permittivity ε_x and the conductivity σ_x by Eqs. (1)–(4). Therein A_x is the cross sectional area of the respective material and L is the length of the columns in the well-defined cermet structure (i.e., the thickness of the porous electrode).

$$r_{x} = \frac{dL}{A_{x} \cdot \sigma_{x}} \tag{1}$$

$$R_{x} = \int_{0}^{L} \frac{dL}{A_{x} \cdot \sigma_{x}} = \frac{L}{A_{x} \cdot \sigma_{x}}$$
 (2)

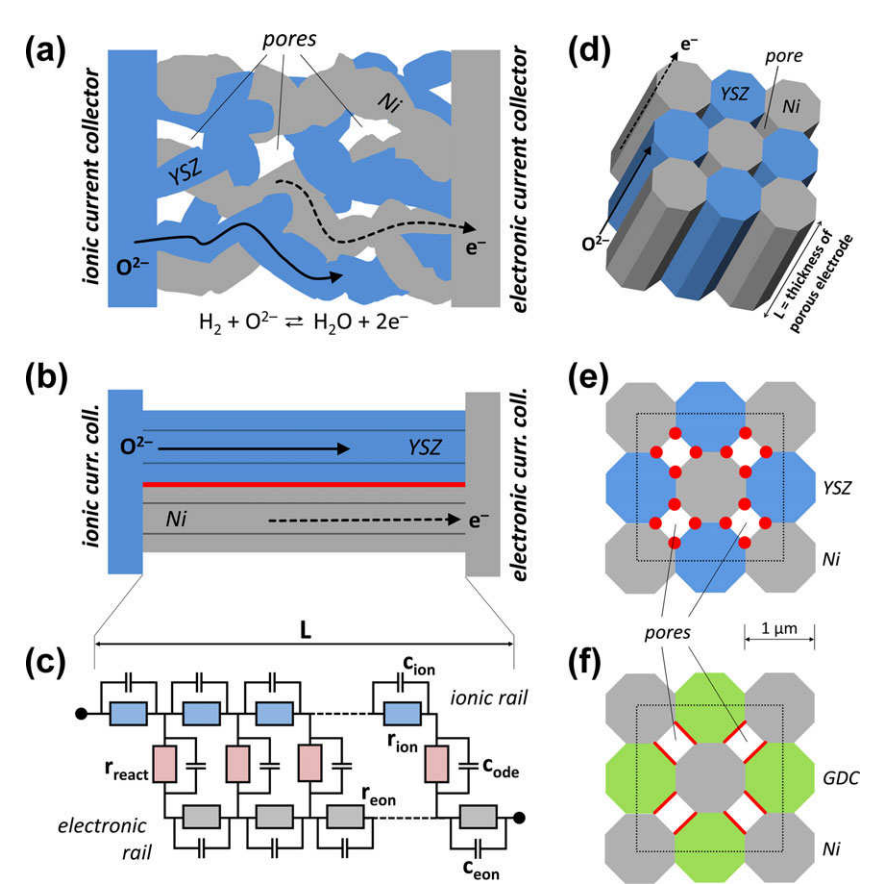


Fig. 2 (a) Sketch of the electrochemical current pathways in a "real" porous Ni/YSZ cermet electrode. Oxygen ions and electrons are restricted to YSZ (blue) and Ni (gray), respectively. The electrochemical reaction is assumed to be restricted to the triple phase boundary (TPB), where YSZ, Ni, and gas phase (i.e., pores) meet. (b) Geometrically simplified picture of the situation in (a): Ion and electron conducting phase are notionally stretched, thus appearing as columns touching each other. The electrochemically active TPB is indicated by the red color. (c) Transmission line circuit describing the current pathways in (a) and (b): Ionic rail (YSZ) and electronic rail (Ni) are connected via the electrochemical reaction at the TPB. (d) 3D sketch of the geometrically simplified cermet in (b). (e) 2D cut through the porous columnar structure in (d) parallel to the current collectors. The electrochemically active zones at the TPB are again highlighted in red. (f) Sketch of the 2D cut from (e) after changing the ion conducting phase from YSZ to gadolinium doped ceria (GDC). Owing to the MIEC properties of GDC the electrochemically active phase extends to its entire free surface.

$$c_{x} = \frac{A_{x} \cdot \varepsilon_{x}}{dL} \tag{3}$$

$$C_{x} = \left(\int_{0}^{L} \frac{dL}{A_{x} \cdot \varepsilon_{x}}\right)^{-1} = \frac{A_{x} \cdot \varepsilon_{x}}{L}$$
(4)

The electric currents along ionic and electronic rail are connected by the electrochemical reaction. In the simplest case, the electrochemical reaction is also characterized by one resistive and one capacitive elementary process. The first originates from the finite electrochemical reaction rate, which is inversely proportional to the electrochemical reaction resistance. The latter emerges from the transient charge transport via the interfacial capacitance. The corresponding geometry-normalized elementary parameters can be obtained for example by impedance measurements on micro-patterned thin film model electrodes [47,51,52]. The differential electrochemical resistor r_{react} and the total reaction resistance of the entire transmission line R_{react} can be obtained from the geometry related electrochemical reaction resistance \hat{R}_{react} by Eqs. (5) and (6), respectively.

$$r_{\text{react}} = \frac{\hat{R}_{\text{react}}}{\Lambda \cdot dL} \tag{5}$$

$$R_{\text{react}} = \left(\int_{0}^{L} \frac{\Lambda \cdot dL}{\hat{R}_{\text{react}}} \right)^{-1} = \frac{\hat{R}_{\text{react}}}{\Lambda \cdot L}$$
 (6)

Here, Λ is the density of electrochemical reaction sites per unit thickness of the porous cermet electrode. (Please note that the unit of \hat{R}_{react} is either Ω cm or Ω cm² for TPB or area active electrodes – cf. Figure 1. Consequently, the unit of Λ is either TPB-length per length or area per length.) These two cases are also sketched by the cross sections of the simplified cermet in Figures 2e and 2f for a TPB and surface active electrode, respectively. In both sketches the electrochemically active regions are highlighted by red color.

Analogously, the differential electrode capacitance c_{ode} and the total electrode capacitance of the entire transmission line C_{ode} are connected by Eqs. (7) and (8) to the geometry related capacitance \hat{C}_{ode} , which can again be obtained from model electrode experiments [53–55].

$$c_{ode} = \hat{C}_{ode} \cdot \Gamma \cdot dL \tag{7}$$

$$C_{\text{ode}} = \int_{0}^{L} \hat{C}_{\text{ode}} \cdot \Gamma \cdot dL = \hat{C}_{\text{ode}} \cdot \Gamma \cdot L$$
 (8)

The factor Γ denotes the contact area between ion and electron conducting phase per unit length of the porous cermet in case of interfacial electrode capacitances. In case of a chemical capacitance – that means a pseudo-capacitance originating for example from the polarization-driven stoichiometry change of a mixed conducting phase [56–58] – it denotes the volume of the respective phase per unit length of cermet electrode.

With these parameters the impedance of the circuit in Figure 2c can be calculated. The general impedance of this type of transmission line can be obtained from the literature – e.g., from papers by Göhr [59] or Bisquert [60]. For the particular case here it reads:

$$\begin{split} Z = & \frac{Z_{ion} \cdot Z_{eon}}{Z_{ion} + Z_{eon}} + \sqrt{(Z_{ion} + Z_{eon}) \cdot Z_{react}} \\ & \cdot \frac{1 + 2 \cdot \frac{Z_{ion} \cdot Z_{eon}}{(Z_{ion} + Z_{eon})^2} \left\{ \sqrt{1 - \left[tanh \left(\sqrt{\frac{Z_{ion} + Z_{eon}}{Z_{react}}} \right) \right]^2 - 1 \right\}}}{tanh \left(\sqrt{\frac{Z_{ion} + Z_{eon}}{Z_{react}}} \right) \end{split}$$

$$Z_{\text{ion}} = \frac{R_{\text{ion}}}{1 + i\omega C_{\text{ion}} R_{\text{ion}}} \tag{10}$$

$$Z_{eon} = \frac{R_{eon}}{1 + i\omega C_{eon} R_{eon}}$$
 (11)

$$Z_{\text{react}} = \frac{R_{\text{react}}}{1 + i\omega C_{\text{ode}} R_{\text{react}}}$$
(12)

In Eqs. (10)–(12) i and ω denote imaginary unit and angular frequency (which is connected to the frequency f by ω = 2 π f), respectively.

It should be emphasized that in literature already various studies can be found with a very similar goal and thus also a similar approach of setting up the electrochemical model. To treat the impedance response of porous electrodes, transmission line circuits have already been suggested in the early works of Gerischer and de Levie [61-64]. General impedance models for transmission line circuits considering two charge carriers and an electrochemical reaction between them were discussed in Refs. [59, 60, 65-69]. For interpreting the impedance of solid mixed ionic and electronic conducting (MIEC) materials, a very similar approach can be found [56, 57]. Moreover, for this type of electrode materials simulation of DC behavior was done by analytical [70] as well as numerical methods [71,72]. The special case for mixed conducting SOFC cathodes can be found in [73,74], while [75] suggests a calculation method also including gas diffusion in the pores of a porous mixed conductor. A very similar approach was used for composite cathodes consisting of a pure ionic and a predominantly electronic conducting phase [76,77]. Moreover, also models for simulation of cermet-type electrodes are based on the same principle of calculating the transmission line circuit like the studies mentioned above [11, 17, 78–81].

In the present work the impedance of SOFC cermet anodes is simulated by means of a transmission line circuit, with elementary parameters being obtained from model-type experiments. The calculation approach allows a systematic and independent variation of these elementary parameters to identify the sensitivity of the polarization resistance of this type of porous SOFC electrodes on the individual properties of the materials in the cermet.

3 Results and Discussion

3.1 Modeling Results and Discussion of Parameter Variation

In the first step, the model introduced above is used to calculate the impedance of a Ni/YSZ cermet at a temperature of $750\,^{\circ}\mathrm{C}$ in a frequency range of $10\,\mathrm{mHz}$ to $1\,\mathrm{MHz}$. For this means, the elementary parameters in Table 1 are used. (Please note that for Ni, since it is a metal rather than a classical dielectric, its capacitive effect was neglected in the simulations here.) The geometry factors, which are needed to convert the elementary parameters in resistances and capacitances (cf. Eqs. (1)–(4)), are obtained from the geometrically well-defined cermet struc-

Table 1 Elementary parameters used for simulation of a Ni/YSZ cermet at 750 °C.

Parameter	Value	Reference; Comment
Ionic conductivity of YSZ, σ_{ion}	0.015 S cm ⁻¹	[83]
Electronic conductivity of Ni, σ_{eon}	10 ⁵ S cm ⁻¹	approximate value
Reaction resistance, \hat{R}_{react}	$10^6\Omega$ cm	[21,51,78]; mean literature value for $p(H_2):p(H_2O) \approx 10$
Permittivity of YSZ $(\varepsilon = \varepsilon_R \cdot \varepsilon_0)$	25·8.85·10 ⁻¹⁴ F cm ⁻¹	[90, 91]
Electrode capacitance	$300~\mu F~cm^{-2}$	[53,92]

Table 2 Geometry factors for $1\,\mathrm{cm}^2$ of geometrically well-defined Ni/YSZ cermet electrode.

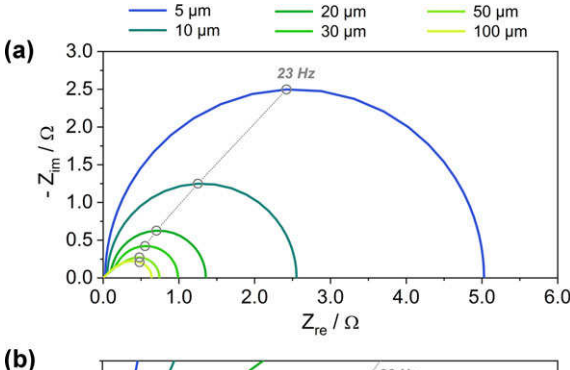
Geometry factor	Value
Area of ion conducting phase, A _{ion}	0.414 cm ²
Area of electron conducting phase, $\boldsymbol{A}_{\text{eon}}$	0.414 cm^2
Contact area between ion and electron conducting phase, $\boldsymbol{\Gamma}$	8,284 cm ² cm ⁻¹
TPB-length density, Λ	$4{\cdot}10^8~\mathrm{cm}~\mathrm{cm}^{-1}$

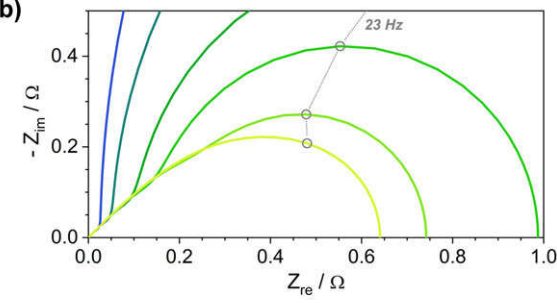
ture shown in Figures 2d and 2e, and are summarized for 1 cm^2 projected area of this porous cermet electrode in Table 2.

3.1.1 Thickness Variation

In Figures 3a and 3b the obtained impedance spectra are depicted for varying thickness L of 1 cm² of the well-defined porous Ni/YSZ electrode. From these Nyquist plots it can be seen that not only the total size of the simulated spectra decreases with increasing thickness, but also their shape. For the thinnest simulated electrode it consists of a small 45° feature at high frequencies and an almost ideal semicircle at low frequencies. With increasing thickness the spectrum transforms into a teardrop-like feature with a more pronounced 45° slope at higher frequencies and a less pronounced low frequency semicircle. The transition between these two types of spectra is determined by the electrochemically active length $\lambda = \sqrt{\hat{R}_{react}\sigma_{ion}A_{ion}/\Lambda}$ of the cermet. For electrodes thinner than λ the spectrum is semicircle-like whereas for electrodes thicker than λ the teardrop-shaped spectrum results. For the relatively coarse Ni/YSZ (without tortuosity) calculated here (see Figure 2d) the electrochemically active length is ca. 39 μm, which is also reflected by the change of the shape of spectra when increasing the electrode thickness from 30 to 50 µm, cf. Figure 3b.

In [60] the more pronounced 45° feature is explained by the increased resistance of charge transport along the rails (cf. Figure 2c) for thicker electrodes, while simultaneously the total reaction resistance decreases. For the system Ni/YSZ simulated here this means that the 45° feature is predominantly affected by the ionic conductivity of YSZ (since the electronic conductivity of Ni is orders of magnitude larger its effect is





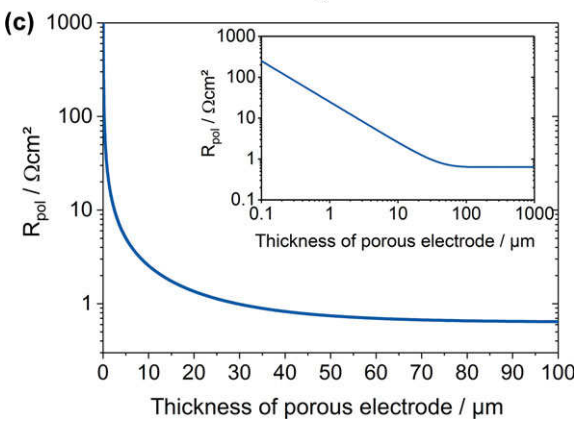


Fig. 3 (a) Nyquist plot of impedance spectra calculated by Eqs. (9)–(12) using the elementary parameters and geometry data from Tables 1 and 2 for varying thickness L of the synthetic cermet in Figure 2d. (b) Zoom of (a). (c) Low frequency axis intercept (i.e., DC polarization resistance R_{pol}) of the spectra in (a) plotted logarithmically versus the thickness of the porous electrode. The inset shows the same curve in a double logarithmic plot.

negligible – see also Section 3.2 below) and the semicircle like feature is caused to a large extent by the reaction resistance. The associated capacitance is virtually only the electrode capacitance since the dielectric capacitance of YSZ is too small to be visible in the considered frequency range. The interpretation of the 45° slope and the semicircle like feature will be further discussed in terms of a parameter variation in the following sections.

In addition to the Nyquist plots, the low frequency axis intercept, which represents the DC polarization resistance of the respective cermet, is plotted as a function of electrode thickness in Figure 3c. The obtained curve depicts that increasing the electrode thickness up to the electrochemically active length λ shows a strong effect on the polarization resistance. For thicker electrodes, however, a further increase of thickness

has only very small effects. Thus, for the geometrically well-defined porous cermet the practical electrochemical utilization depth is around $40\text{--}50\,\mu\text{m}$. Consequently, the part of the electrode beyond that thickness is electrochemically inactive. Please note that for a real cermet the electrode layer thickness is expected to be about a factor 2–3 smaller than the effective ion travel distance due to tortuosity of the YSZ phase.

3.1.2 Variation of Ionic and Electronic Conductivity

Figure 4 shows the simulation results for a variation of the ionic conductivity $\sigma_{\rm ion}$, while all the other elementary parameters are kept constant. In Figures 4a and 4b the spectra for a constant thickness of $30\,\mu m$ are plotted with the blue dotted curve indicating the original spectrum from Figure 3a (i.e., with elementary parameters from Table 1). In accordance with the above mentioned interpretation, the 45° feature becomes

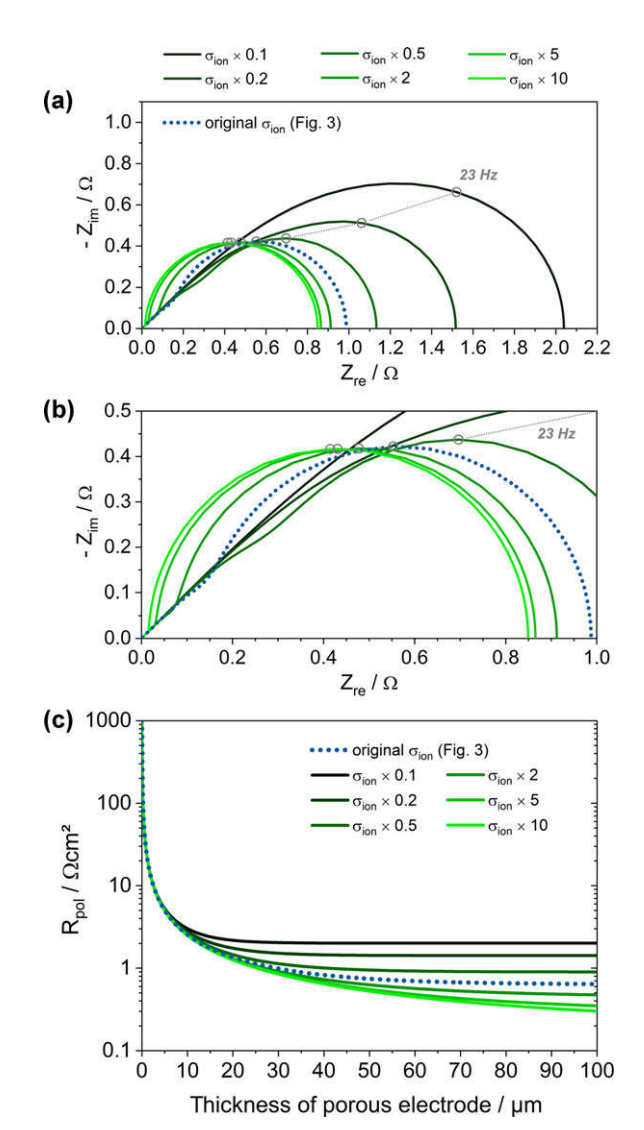


Fig. 4 (a) Impedance spectra (Nyquist plot) for a constant electrode thickness of 30 μm but varying conductivity of the ionic rail. (b) Zoom of (a). (c) Dependence of DC polarization resistance as a function of electrode thickness for varying ionic conductivity. The blue dotted line is the curve from Figure 3c.

less pronounced for the simulation with higher ionic conductivity. In case of lower ionic conductivity the spectra become teardrop-like with a larger 45° feature. The larger semicircle-like feature in this case can also be understood when looking at the corresponding decay curves of the DC polarization resistance in Figure 4c. The smaller the ionic conductivity, the shorter is the electrochemically active region. Consequently, less TPB is electrochemically active resulting in an absolutely larger reaction resistance than in case of high ionic conductivity, which can be seen in Figures 4a and 4b.

A variation of the electronic conductivity σ_{eon} leads to much less pronounced changes in the electrode behavior. Since the conductivity of metallic Ni is very high, also changes by orders of magnitude do not efficiently affect the electrode behavior as can be seen from the plots of the DC polarization resistance *versus* electrode thickness in Figure 5. Only if the electronic conductivity comes rather close to the value of the ionic conductivity an effect becomes visible. For the curve with $10^{-7}\times\sigma_{eon}$ (= 0.01 Scm⁻¹; cf. Table 1) a significant increase of the DC polarization resistance occurs for electrode thicknesses larger than ca. 30–40 µm. Again the electrode is not electrochemically active for thicknesses larger than this value. But in addition to the situation above, the rather low electronic conductivity leads to an additional resistance for electrode material beyond the utilization length.

For a practical application the following conclusion can be drawn from this result: Given a sufficient electronic current collection – that means that the electron conductor in the composite is not needed for carrying a lateral current – an electronic conductivity being about one order of magnitude larger than the ionic conductivity is way enough to avoid a detrimental effect on the total polarization resistance of the composite electrode. Thus, also electron conducting oxides can be a valid choice for composite electrodes [82]. Of course, effects of changes in catalytic activity or changes in microstructure, which may very likely be associated with such an exchange of a metal against an electron conducting oxide, cannot be evaluated from the results in Figure 5. The influence of catalytic activity of the two materials or their combination on the total polarization resistance is discussed in the following section.

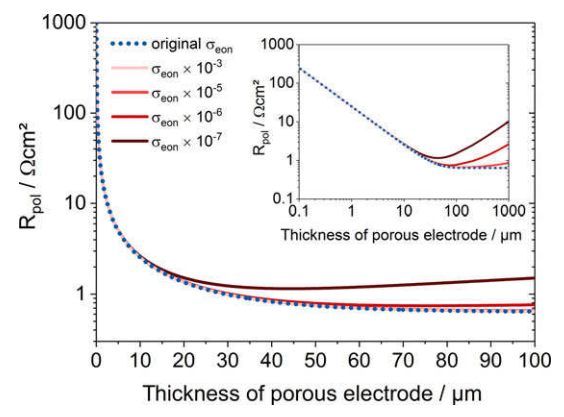


Fig. 5 Plot of the DC polarization resistance as a function of electrode thickness and for different conductivities of the electronic rail.

3.1.3 Variation of Electrochemical Reaction Resistance

The results of the variation of the electrochemical reaction resistance \hat{R}_{react} are shown in Figure 6. Here, a qualitatively similar picture than for the ionic conductivity can be found (see Figures 6a and 6b and compare with Figures 4a and 4b). For higher reaction resistances and thus lower electrochemical activity the spectra consist of a small 45° feature at high frequencies and a relatively large semicircle in the low frequency region. In case of lower reaction resistances (i.e., higher electrochemical activity) the spectra turn into teardrop-shaped features. From a quantitative point of view, however, the variation of the reaction resistance shows a much stronger effect than changes of ionic conductivity. This becomes even more obvious when looking at the plot of the DC polarization resistance as a function of electrode thickness (cf. Figure 6c). The

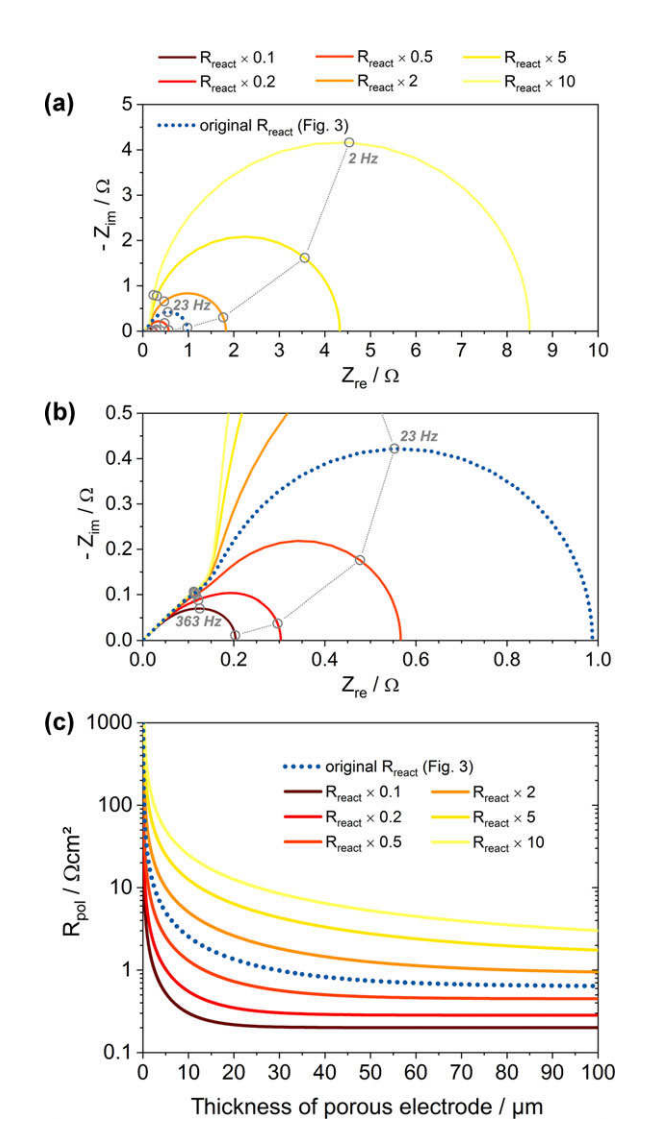


Fig. 6 (a) Impedance spectra (Nyquist plot) for a constant electrode thickness of 30 μ m but varying reaction resistance (i.e., electrochemical activity). (b) Zoom of (a). (c) Dependence of DC polarization resistance as a function of electrode thickness for varying R_{react} . The blue dotted line is the curve from Figure 3c.

variation of $R_{\rm react}$ by two orders of magnitude affects the DC polarization resistance by one to almost two orders of magnitude, depending on electrode thickness. Therefore, the variation of the electrochemical reaction resistance is the most effective screw one can turn to increase the electrochemical performance of a cermet electrode.

The effect that for smaller reaction resistances the 45° feature, which was above interpreted to be predominantly affected by the ionic conductivity, also becomes smaller can also be understood when looking at the decay curves of the DC polarization resistance in Figure 6c. For small \hat{R}_{react} the utilization depth of the cermet becomes significantly shorter. Therefore, ions travel shorter distances in the ionic rail, which leads to a smaller 45° feature in the Nyquist plot (see Figure 6b).

3.1.4 Material Variation

In contrast to the rather synthetic variation of only one elementary parameter, a possible "real world" scenario is the change of one material against another one. As already mentioned in Section 1, Ni/ceria based cermets were proposed in recent years to offer a potentially better performing alternative to Ni/YSZ. The reason for the usually higher performance of Ni/ceria cermets is not completely understood so far. In literature the higher ionic conductivity and the higher electrochemical activity of GDC and SDC as well as the different microstructure of the ceria based cermet are discussed as potential reasons. A clear separation of these effects, however, is not straightforwardly possible since on real cermets usually all three properties are affected by an exchange of YSZ against GDC. The advantage of the simulations in this study is that such a material exchange can be done without affecting the microstructure of the cermet. For substitution of YSZ by GDC the corresponding elementary parameters as well as some geometry factors need to be adapted in the calculations. First, the ionic conductivity of GDC is higher than that of YSZ. Second, owing to the mixed conductivity of the material, the electrochemical reaction proceeds on the entire free GDC surface rather than only at the TPB. Third, the source of the capacitance of these electrodes is mainly the chemical capacitance of GDC, which is significantly larger than the interfacial capacitance. The respective parameters used for simulating the impedance of a Ni/GDC cermet electrode at 750 °C are summarized in Tables 3 and 4.

The simulation result for a 30 μ m thick Ni/GDC cermet is compared in Figure 7 with the Ni/YSZ result (from Figure 3). The impedance spectra in Figure 7a directly reflect the higher conductivity of GDC by the smaller 45° high frequency feature. Moreover, the smaller low frequency arc as well as the smaller total impedance indicate that for the given geometry of the cermet surface active GDC is indeed better performing than TPB-active Ni/YSZ. From the decay curves of the DC polarization resistance in Figure 7b one can also deduce that the utilization length of Ni/GDC is larger than of Ni/YSZ. If we define the utilization length as the thickness of the cermet, which leads to a polarization resistance 10% larger than the

Table 3 Elementary parameters used for simulation of a Ni/GDC cermet at $750\,^{\circ}\text{C}$.

Parameter	Value	Reference; Comment
Ionic conductivity of GDC, σ_{ion}	0.06 S cm ⁻¹	[43,93,94]
Electronic conductivity of Ni, σ_{eon}	10 ⁵ S cm ⁻¹	approximate value
Reaction resistance, \hat{R}_{react}	$10\Omega \text{ cm}^2$	[47,95]
Permittivity of GDC ($\epsilon = \epsilon_R \cdot \epsilon_0$)	25·8.85·10 ⁻¹⁴ F cm ⁻¹	assumed to be equal to YSZ
Chemical capacitance of GDC, \hat{C}_{ode}	700 F cm ⁻³	[95]

Table 4 Geometry factors for 1 cm² of geometrically well-defined Ni/GDC cermet electrode (cf. Figure 2f).

Geometry factor	Value
Area of ion conducting phase, A _{ion}	0.414 cm^2
Area of electron conducting phase, $\boldsymbol{A}_{\text{eon}}$	0.414 cm^2
Volume density of the GDC phase, $\boldsymbol{\Gamma}$	$0.414~{\rm cm^3~cm^{-1}}$
Surface area density, Λ	$8,284 \text{ cm}^2 \text{ cm}^{-1}$

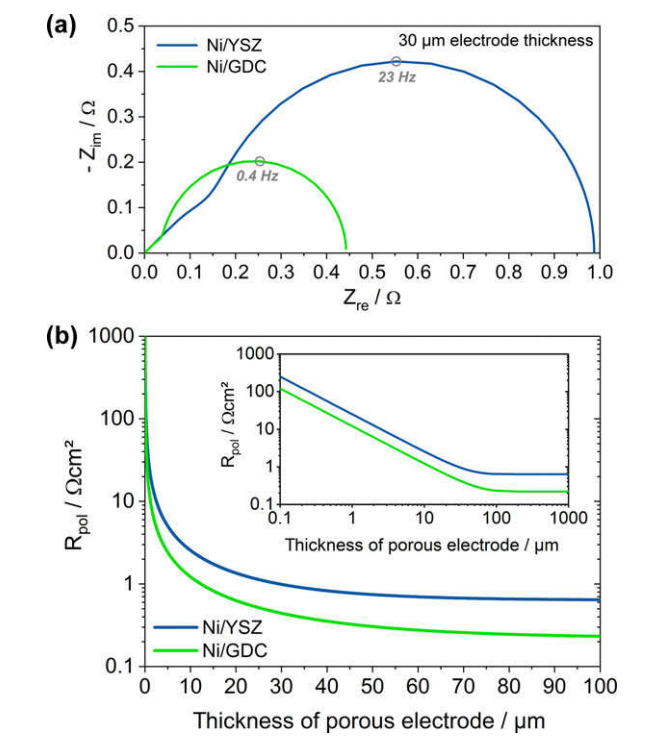


Fig. 7 (a) Simulated impedance spectra (Nyquist plot) of a Ni/YSZ and a Ni/GDC cermet with identical microstructure (cf. Figures 2e and 2f) and $30\mu m$ thickness. (b) Decay curves of the DC polarization resistance of both cermets.

lowest possible $R_{\rm pol}$ (i.e., a thickness allowing 90% of the theoretically possible electrode performance) we obtain values of 59 and 83 μm for Ni/YSZ and Ni/GDC, respectively. For practical application this result means that Ni/GDC anodes of similar microstructure than Ni/YSZ anodes need to be prepared thicker to exploit their full potential.

3.2 Experimental Verification of the Model

To exemplarily demonstrate the practical applicability of the transmission line model discussed above, this equivalent circuit was employed to fit impedance spectra measured on real porous Ni/YSZ cermet electrodes. Electrolyte-supported model cells with symmetric, macroscopically extended Ni/YSZ cermet electrodes ($9 \times 9 \, \text{mm}^2$) were prepared by screen printing Ni/YSZ paste on $8 \, \text{mol.}\%$ YSZ foils ($10 \times 10 \, \text{mm}^2$) followed by sintering for $3 \, \text{h}$ at $1,200 \, ^{\circ}\text{C}$ in hydrogen atmosphere. A detailed description of Ni/YSZ paste and model cell preparation as well as of the electrochemical measurement procedure can be found in Refs. [10] and [12].

A typical impedance spectrum measured at $740\,^{\circ}\text{C}$ in an atmosphere containing 25 mbar H_2 and 25 mbar H_2O (balance Ar) is depicted in Figure 8a. The spectrum consists of three

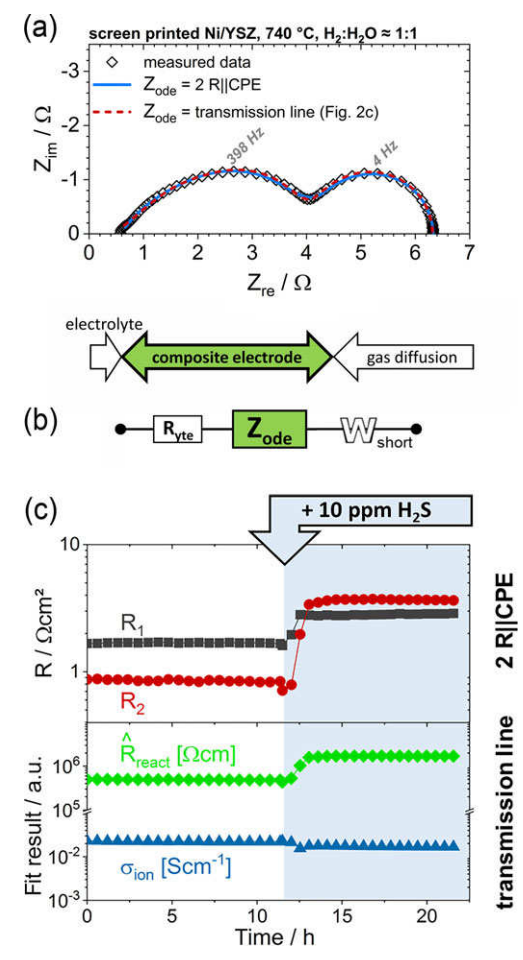


Fig. 8 Comparison of models for fitting the impedance of a screen printed porous Ni/YSZ anode. (a) Impedance spectrum (Nyquist plot, open diamonds) measured at 740 °C in an atmosphere of 25 mbar $\rm H_2$, 25 mbar $\rm H_2O$, balance Ar together with fit results (solid and dashed curves), which were obtained by employing two different models. (b) Equivalent circuit used for fitting. For $\rm Z_{ode}$ the impedance of 2 R | CPE elements and the impedance of the transmission line from Figure 2c (i.e., Eq. (9)) was used, leading to the solid blue and the dashed red spectrum in (a). (c) Plot of the fit parameters obtained by the two different models versus time showing the evolution of the respective parameters upon $\rm H_2S$ addition to the feed gas.

well-separated main features: (i) a high frequency axis intercept corresponding to the ion transport resistance of the electrolyte, (ii) a depressed intermedium frequency feature, which is assigned to the impedance of the composite electrode, and (iii) a low frequency arc due to gas diffusion limitation [12]. These three contributions are also indicated by the arrows below the spectrum in Figure 8a. From the teardrop-like shape of the spectrum part attributed to the cermet electrode, it can already be concluded that the electrode thickness of 15 µm is of the order of the electrochemically active thickness λ (see Section 3.1.1). This lower value for λ compared to the geometrically well-defined structure can be explained by the finer microstructure of the screen printed Ni/YSZ cermet, which effectively leads to a lower value for R_{react}. This conclusion is also supported by the higher peak frequency of the cermet feature in Figure 8a.

In order to prove if the transmission-line circuit suggested in this paper is able to successfully deconvolute the elementary processes of the cermet spectrum, it was fitted to the equivalent circuit in Figure 8b. In this circuit R_{vte} represents the electrolyte resistance (i.e., the high frequency intercept), Z_{ode} the impedance of the composite electrode, and W_{short} is a Warburg element used to fit the gas diffusion impedance at low frequencies. To assess the appropriateness of the transmission line model, two fit procedures were performed. First, for Z_{ode} the impedance of the transmission line discussed in this paper was used (Eqs. (9)–(12)) with R_{ion}, R_{react}, and C_{ode} as fit parameters for an electrode thickness of $15\,\mu m$ [12] (R_{eon} was fixed to 10⁵S cm⁻¹ for Ni; C_{ion} and C_{eon} were neglected, since they are too small to be visible). With this approach the red dashed curve in Figure 8a was obtained. In a second fit, for Z_{ode} the impedance of two serial R | CPE elements was used; CPE is a constant phase element with impedance $Z_{CPE} = Q^{-1}(i\omega)^{-n}$ (Q and n are fit parameters). This approach thus represents the assumption of two processes with two different relaxation times being responsible for the impedance feature of the cermet anode. The corresponding fit result is depicted in Figure 8a with the blue solid curve. Even though the transmission line fit has only four free parameters, the obtained fit quality is virtually equal to the 2R | CPE fit with six free parameters.

The resulting resistive parameters for both models are summarized in Table 5. In this table the parameter $R_{\rm ion}$ was already converted into an ionic conductivity by estimating a cross section area of YSZ $A_{\rm ion}\approx 0.2\,{\rm cm}^2$ per ${\rm cm}^2$ of projected electrode area [12] and an estimated tortuosity factor of ca. 3. The obtained ionic conductivity of ca. $2\times 10^{-2}\,{\rm S~cm}^{-1}$ is in good agreement with the expected bulk value of YSZ (see Table 1

and [83]). Since (yet) no reliable value for the TPB-density of the electrodes is available, the TPB-density of the well-defined cermet in Figure 2 was used (cf. Table 2), which is of the same order of magnitude than values obtained by 3D reconstruction [37]. The obtained fit result for \hat{R}_{react} is

somewhat lower than the average literature value used for the simulations (see Table 2 and [21,51,78]), but this is most likely caused by the underestimation of the TPB density of the cermet electrode by using the data of the well-defined structure. Moreover, this result may also be affected by different impurity levels of the model electrodes and the cermet. Also, a systematic error due to the Warburg element connected in series to the transmission cannot be completely excluded. (Please note that the transmission line fit yields a more accurate R_{vte} than the 2 R \mid CPE fit, but R_{gasdiff} is overestimated.) To obtain more accurate results for σ_{ion} and \hat{R}_{react} the gas diffusion resistance should thus be avoided by optimizing the measurement conditions, which is the focus of a forthcoming paper. Additionally, a three dimensional reconstruction of the cermet [84] would be needed for more accurate geometry parameters such a 3D reconstruction, however, is far beyond the scope of the present work.

To further test the appropriateness of the transmission line model, a sulfur poisoning experiment was conducted by adding 10 ppm H₂S to the feed gas. H₂S is well-known in literature to have a detrimental effect on the H₂ oxidation kinetics of Ni/YSZ based SOFC anodes [1, 30, 51, 85–89]. The physical effect behind H₂S poisoning is discussed to be related to blocking of hydrogen adsorption sites on Ni leading to a decreased reaction rate at the TPB. Thus, for the experiment here, the reaction resistance at the TPB is expected to increase in the presence of H₂S in the feed gas, while the ionic conductivity of YSZ will hardly be affected. The resulting changes of the obtained parameters of both fitting models are shown in Figure 8c. From this figure it can be seen that in case of the transmission line fit only the reaction resistance is affected by H₂S, whereas the ionic conductivity is virtually unaffected, which nicely matches the expected behavior. In case of the 2R | CPE fit, however, both resistances significantly change. For the current case of sulfur poisoning such a model could thus lead to the delusive conclusion of two elementary processes being affected by H₂S in the fuel gas.

From these results it can be concluded that the transmission line circuit discussed in this paper is indeed an appropriate model for a physically correct description of the impedance of cermet electrodes. In contrast, a fitting model based on $R \mid CPE$ elements – i.e., on the analysis of different relaxation times – is not feasible for delivering a physically correct description of the elementary processes in a cermet electrode.

Table 5 Results of fitting the spectrum in Figure 8a to the circuit in Figure 8b using either $2 R \mid CPE$ elements or the impedance of the transmission line (Eq. (9)) for the element Z_{ode} .

	R_{yte} / Ω	$\sigma_{ion} / \Omega^{-1} cm^{-1}$	\hat{R}_{react} / Ω cm	R_1 / Ω	R_2 / Ω	$R_{gasdiff}$ / Ω
transmission line fit	0.51	7.7×10^{-3}	1.7×10^{5}			1.35
2 R CPE fit	0.62			2.06	1.08	2.56

cross section area of electron conductor

4 Conclusions

Simulations of the polarization resistance of a porous cermet electrode were done based on an equivalent circuit representing the physically correct connection of electrochemical elementary processes. The corresponding elementary parameters for calculations were taken from model type measurements. The used simulation approach allows independent variation of the elementary parameters such as ionic and electronic conductivity as well as reaction resistance to analyze the influence of the respective parameter on the polarization resistance of a porous cermet electrode. The strongest effect on the polarization resistance was found for variation of the reaction resistance thus identifying it as the most effective parameter for optimizing the electrochemical performance of cermet electrodes. The electronic conductivity was revealed to play only a role in case it comes close to the value of the ionic conductivity. Consequently, cermet electrodes with electronic current collectors with much lower conductivity than metals can be sufficient for a well performing cermet electrode, provided that ionic conductivity and reactivity are not affected by such a material exchange.

Substituting YSZ by GDC without changing the microstructure of the porous cermet structure yielded a lower polarization resistance. This decrease of the resistance can be explained to a large part by the increased electrochemical activity of the Ni/GDC cermet compared with Ni/YSZ and to a smaller part by the higher ionic conductivity of GDC. Moreover, the decay length of the electrochemical activity was found to be larger for Ni/GDC, which indicates that Ni/GDC anodes need to be prepared thicker than usual Ni/YSZ anodes to exploit the full potential of the ceria based cermet.

In addition to the modeling approach, the transmission line circuit was also used in a first attempt to fit impedance data measured on real porous Ni/YSZ cermet electrodes. The response of the ionic conductivity in the YSZ phase of the cermet and the electrochemical reaction resistance at the TPB upon H_2S exposure was compared to the behavior of resistances obtained by a fitting approach based on $2\,R\,\big|\,$ CPE elements (i.e., on different relaxation times). In this H_2S poisoning experiment, the transmission line fit yielded the expected behavior of only the reaction resistance to increase upon hydrogen sulfide addition, while the fit based on $R\,\big|\,$ CPE elements suggested two resistive processes to be affected.

Acknowledgements

The financial support by the Austrian Federal Ministry for Digital and Economic Affairs and the National Foundation for Research, Technology and Development is gratefully acknowledged. The authors acknowledge the TU Wien University Library for financial support through its Open Access Funding Programme. Moreover, we thank Dr. Veronika Rojek-Wöckner for providing the screen printed Ni/YSZ cermet samples.

List of Symbols

A_{ion}	cross section area of ion conductor
Ceon	differential capacitance of the electron conductor
Cion	differential capacitance of the ion conductor
c _{ode}	differential electrode capacitance
C_{eon}	capacitance of the electron conductor
C_{ion}	capacitance of the ion conductor
C_{ode}	electrode capacitance
Ĉ	geometry related electrode capacitance
ϵ_{eon}	permittivity of the electron conductor
ϵ_{ion}	permittivity of the ion conductor
f	frequency
i	imaginary unit $(=\sqrt{-1})$
Γ	contact area between ion and electron conducting
	phase or volume density of mixed conducting phase
L	thickness of cermet electrode
Λ	TPB-length density or surface area density
r_{eon}	differential resistance of electron conductor
r_{ion}	differential resistance of ion conductor
r_{react}	differential electrochemical reaction resistance
R_{eon}	resistance of electron conductor
Rion	resistance of ion conductor
R_{react}	electrochemical reaction resistance
\hat{R}_{react}	geometry related electrochemical reaction resistance
R_{pol}	DC polarization resistance
σ_{eon}	electronic conductivity
σ_{ion}	ionic conductivity
ω	angular frequency
Z	impedance of the cermet
Z_{ion}	impedance of ion conducting rail

References

Zeon

 Z_{react}

[1] K. Haga, S. Adachi, Y. Shiratori, K. Itoh, K. Sasaki, *Solid State Ionics* **2008**, 179, 1427.

impedance of electron conducting rail

impedance of electrochemical reaction

- [2] C. Graves, S. D. Ebbesen, M. Mogensen, K. S. Lackner, Renewable Sustainable Energy Rev. 2011, 15, 1.
- [3] A. Hauch, K. Brodersen, M. Chen, M. B. Mogensen, *Solid State Ionics* **2016**, 293, 27.
- [4] A. Weber, E. Ivers-Tiffée, J. Power Sources 2004, 127, 273.
- [5] A. Atkinson, S. Barnett, R. J. Gorte, J. T. S. Irvine, A. J. McEvoy, M. Mogensen, S. C. Singhal, J. Vohs, *Nat. Mater.* 2004, 3, 17.
- [6] M. D. Gross, J. M. Vohs, R. J. Gorte, J. Mater. Chem. 2007, 17, 3071.
- [7] D. J. L. Brett, A. Atkinson, N. P. Brandon, S. J. Skinner, Chemical Society Reviews 2008, 37, 1568.
- [8] S. C. Singhal, Solid State Ionics 2002, 152–153, 405.
- [9] M. C. Tucker, G. Y. Lau, C. P. Jacobson, L. C. DeJonghe,S. J. Visco, J. Power Sources 2007, 171, 477.

- [10] M. Rüttinger, R. Mücke, T. Franco, O. Büchler, N. H. Menzler, A. Venskutonis, ECS Trans. 2011, 35, 259.
- [11] J. Nielsen, T. Klemensø, P. Blennow, J. Power Sources **2012**, 219, 305.
- [12] V. A. Rojek-Wöckner, A. K. Opitz, M. Brandner, J. Mathé, M. Bram, J. Power Sources 2016, 328, 65.
- [13] H. Sumi, H. Shimada, Y. Yamaguchi, T. Yamaguchi, J. Electrochem. Soc. 2017, 164, F243.
- [14] A. Hauch, S. D. Ebbesen, S. H. Jensen, M. Mogensen, *J. Electrochem. Soc.* **2008**, 155, B1184.
- [15] R. D. Green, C.-C. Liu, S. B. Adler, Solid State Ionics 2008, 179,647.
- [16] J.-h. Myung, D. Neagu, D. N. Miller, J. T. S. Irvine, Nature **2016**, 537, 528.
- [17] S. Dierickx, T. Mundloch, A. Weber, E. Ivers-Tiffée, ECS Trans. 2017, 78, 1273.
- [18] J. W. Yun, S. P. Yoon, S. Park, H. S. Kim, S. W. Nam, Int. J. Hydrogen Energy 2011, 36, 787.
- [19] D. K. Niakolas, Appl. Catal. A 2014, 486, 123.
- [20] M. Haydn, K. Ortner, T. Franco, N. H. Menzler, A. Venskutonis, L. S. Sigl, Powder Metallurgy 2013, 56, 382.
- [21] J. Mizusaki, H. Tagawa, T. Saito, K. Kamitani, T. Yamamura, K. Hirano, S. Ehara, T. Takagi, T. Hikita, M. Ippommatsu, S. Nakagawa, K. Hashimoto, J. Electrochem. Soc. 1994, 141, 2129.
- [22] A. Bieberle, L. P. Meier, L. J. Gauckler, J. Electrochem. Soc. 2001, 148, A646.
- [23] W. Yao, E. Croiset, J. Power Sources 2013, 226, 162.
- [24] W. G. Bessler, M. Vogler, H. Stormer, D. Gerthsen, A. Utz, A. Weber, E. Ivers-Tiffee, Phys. Chem. Chem. Phys. 2010, 12, 13888.
- [25] A. Utz, H. Störmer, A. Leonide, A. Weber, E. Ivers-Tiffee, ECS Trans. 2009, 25, 2013.
- [26] A. Utz, H. Störmer, A. Leonide, A. Weber, E. Ivers-Tiffée, J. Electrochem. Soc. 2010, 157, B920.
- [27] A. K. Opitz, M. Kubicek, S. Huber, T. Huber, G. Holzlechner, H. Hutter, J. Fleig, J. Mater. Res. 2013, 28, 2085.
- [28] J. Fleig, F. S. Baumann, V. Brichzin, H.-R. Kim, J. Jamnik, G. Cristiani, H.-U. Habermeier, J. Maier, Fuel Cells 2006, 6, 284.
- [29] S. P. Jiang, S. P. S. Badwal, Solid State Ionics 1999, 123,
- [30] Y. Matsuzaki, I. Yasuda, Solid State Ionics 2000, 132, 261.
- [31] A. Weber, B. Sauer, A. C. Müller, D. Herbstritt, E. Ivers-Tiffée, Solid State Ionics 2002, 152-153, 543.
- [32] M. Brown, S. Primdahl, M. Mogensen, J. Electrochem. Soc. 2000, 147, 475.
- [33] S. Primdahl, M. Mogensen, J. Electrochem. Soc. 1997, 144,
- [34] P. Holtappels, I. C. Vinke, L. G. J. de Haart, U. Stimming, I. Electrochem. Soc. 1999, 146, 2976.
- [35] V. Sonn, A. Leonide, E. Ivers-Tiffée, J. Electrochem. Soc. 2008, 155, B675.
- [36] D. Kennouche, Y.-c. K. Chen-Wiegart, C. Riscoe, J. Wang, S. A. Barnett, J. Power Sources 2016, 307, 604.

- [37] J. R. Wilson, S. A. Barnett, Electrochem. Solid-State Lett. **2008**, 11, B181.
- [38] B. A. Boukamp, M. Verbraeken, D. H. A. Blank, P. Holtappels, Solid State Ionics 2006, 177, 2539.
- [39] S. Gewies, W. G. Bessler, J. Electrochem. Soc. 2008, 155, B937.
- [40] E. P. Murray, T. Tsai, S. A. Barnett, Nature 1999, 400, 649.
- [41] O. A. Marina, C. Bagger, S. Primdahl, M. Mogensen, Solid State Ionics 1999, 123, 199.
- [42] S. Park, J. M. Vohs, R. J. Gorte, Nature 2000, 404, 265.
- [43] J. B. Goodenough, Annu. Rev. Mater. Res. 2003, 33, 91.
- [44] N. P. Brandon, S. Skinner, B. C. H. Steele, Annu. Rev. Mater. Res. 2003, 33, 183.
- [45] H. L. Tuller, A. S. Nowick, J. Electrochem. Soc. 1975, 122,
- [46] J. H. Park, R. N. Blumenthal, J. Electrochem. Soc. 1989, 136, 2867.
- [47] W. C. Chueh, Y. Hao, W. Jung, S. M. Haile, Nat. Mater. **2012**, 11, 155.
- [48] W. C. Chueh, W. Lai, S. M. Haile, Solid State Ionics 2008, 179, 1036.
- [49] A. Nenning, E. Navickas, P. Velicsanyi, A. K. Opitz, H. Hutter, J. Fleig, Solid State Ionics 2015, 273, 25.
- [50] V. Esposito, D. W. Ni, Z. He, W. Zhang, A. S. Prasad, J. A. Glasscock, C. Chatzichristodoulou, S. Ramousse, A. Kaiser, Acta Materialia 2013, 61, 6290.
- [51] M. C. Doppler, J. Fleig, M. Bram, A. K. Opitz, J. Power Sources 2018, 380, 46.
- [52] J. Fleig, Solid State Ionics 2003, 161, 279.
- [53] M. C. Doppler, J. Fleig, M. Bram, A. K. Opitz, J. Electrochem. Soc. 2016, 163, H1019.
- [54] A. K. Opitz, J. Fleig, Solid State Ionics 2010, 181, 684.
- [55] W. C. Chueh, S. M. Haile, Phys. Chem. Chem. Phys. 2009, 11,8144.
- [56] J. Jamnik, Solid State Ionics **2003**, 157, 19.
- J. Jamnik, J. Maier, Phys. Chem. Chem. Phys. 2001, 3, 1668.
- [58] W. Lai, S. M. Haile, Journal of the American Ceramic Society 2005, 88, 2979.
- [59] H. Göhr, Electrochemical Applications 1997, 1, 2.
- [60] J. Bisquert, Phys. Chem. Chem. Phys. 2000, 2, 4185.
- [61] H. Gerischer, Zeitschrift fuer Physikalische Chemie 1952, 201, 55.
- [62] H. Gerischer, Zeitschrift fuer Physikalische Chemie 1951, 198, 286.
- [63] R. de Levie, *Electrochim*. *Acta* **1964**, 9, 1231.
- [64] R. de Levie, Electrochim. Acta 1963, 8, 751.
- [65] J. Bisquert, G. Garcia-Belmonte, F. Fabregat-Santiago, A. Compte, Electrochemistry Communications 1999, 1, 429.
- [66] M. Adamič, S. D. Talian, A. R. Sinigoj, I. Humar, J. Moškon, M. Gaberšček, J. Electrochem. Soc. 2019, 166, A5045.
- J. Huang, J. Zhang, J. Electrochem. Soc. 2016, 163, A1983. [67]
- A. Lasia, ECS Trans. 2008, 13, 1.
- [69] U. Tröltzsch, O. Kanoun, Electrochim. Acta 2012, 75, 347.
- H. Deng, M. Zhou, B. Abeles, Solid State Ionics 1994, 74, [70] 75.
- [71] J. Fleig, Annu. Rev. Mater. Res. 2003, 33, 361.

Fuel Cells

- [72] J. Fleig, J. Power Sources 2002, 105, 228.
- [73] S. B. Adler, J. A. Lane, B. C. H. Steele, J. Electrochem. Soc. 1996, 143, 3554.
- [74] S. B. Adler, Solid State Ionics 1998, 111, 125.
- [75] A. J. Samson, M. Søgaard, P. V. Hendriksen, *Electrochim. Acta* 2017, 229, 73.
- [76] J. Nielsen, T. Jacobsen, M. Wandel, *Electrochim. Acta* 2011, 56, 7963.
- [77] J. Nielsen, J. Hjelm, Electrochim. Acta 2014, 115, 31.
- [78] A. Utz, J. Joos, A. Weber, E. Ivers-Tiffée, ECS Trans. 2011, 35, 1669.
- [79] M. Kishimoto, H. Iwai, M. Saito, H. Yoshida, J. Power Sources 2011, 196, 4555.
- [80] Z. Gao, H. Wang, E. Miller, Q. Liu, D. Senn, S. Barnett, ACS Appl. Mater. Interfaces 2017, 9, 7115.
- [81] Z. Gao, L. V. Mogni, E. C. Miller, J. G. Railsback, S. A. Barnett, *Energy and Environmental Science* **2016**, *9*, 1602.
- [82] M. Gerstl, A. Hutterer, J. Fleig, M. Bram, A. K. Opitz, Solid State Ionics 2016, 298, 1.
- [83] C. Ahamer, A. K. Opitz, G. M. Rupp, J. Fleig, J. Electrochem. Soc. 2017, 164, F790.
- [84] J. R. Wilson, A. T. Duong, M. Gameiro, H.-Y. Chen, K. Thornton, D. R. Mumm, S. A. Barnett, *Electrochemistry Communications* 2009, 11, 1052.

- [85] Z. Cheng, M. Liu, Solid State Ionics 2007, 178, 925.
- [86] Z. Cheng, J.-H. Wang, Y. Choi, L. Yang, M. C. Lin, M. Liu, Energ. Environ. Sci. 2011, 4, 4380.
- [87] R. Mukundan, E. L. Brosha, F. H. Garzon, Electrochem. Solid-State Lett. 2004, 7, A5.
- [88] J. F. B. Rasmussen, A. Hagen, J. Power Sources 2009, 191, 534.
- [89] P. Steiger, D. Burnat, H. Madi, A. Mai, L. Holzer, J. Van Herle, O. Kröcher, A. Heel, D. Ferri, *Chem. Mat.* 2019, 31, 748.
- [90] G. Chiodelli, A. Magistris, M. Scagliotti, F. Parmigiani, *Journal of Materials Science* **1988**, 23, 1159.
- [91] M. Hartmanova, K. Gmucova, I. Thurzo, Solid State Ionics 2000, 130, 105.
- [92] M. C. Doppler, J. Fleig, A. K. Opitz, ECS Trans. 2015, 68, 1383.
- [93] M. Mogensen, N. M. Sammes, G. A. Tompsett, Solid State Ionics 2000, 129, 63.
- [94] T. S. Zhang, J. Ma, H. Cheng, S. H. Chan, Materials Research Bulletin 2006, 41, 563.
- [95] M. Gerstl, A. Nenning, R. Iskandar, V. Rojek-Wöckner, M. Bram, H. Hutter, A. K. Opitz, *Materials* 2016, 9, 649.